Physical properties of the layered f-electron van der Waals magnet Ce$_2$Te$_5$

Yu Liu (刘育) ⓘ, M. M. Bordelon ⓘ, A. Weiland ⓘ, P. F. S. Rosa, S. M. Thomas ⓘ, J. D. Thompson, F. Ronning, and E. D. Bauer

MPA-Q, Los Alamos National Laboratory, Los Alamos, New Mexico 87545, USA

We report a detailed study of the magnetic, transport, and thermodynamic properties of Ce$_2$Te$_5$ single crystals, a layered f-electron van der Waals magnet. Four consecutive transitions at ∼5.2, 2.1, 0.9, and 0.4 K were observed in the ac-plane electrical resistivity $\rho(T)$, which were further confirmed in specific heat $C_p(T)$ measurements. Analysis of the magnetic susceptibility $\chi(T)$, the magnetic-field variation of $\rho(T)$, and the increase of the first transition temperature ($T_c \sim 5.2$ K) with applied magnetic field indicates ferromagnetic order, while the decrease of the other transitions with field suggests different states with dominant antiferromagnetic interactions below $T_2 \sim 2.1$ K, $T_3 \sim 0.9$ K, and $T_4 = 0.4$ K. Critical behavior analysis around T_c that gives critical exponents $\beta = 0.31(2)$, $\gamma = 0.99(2)$, $\delta = 4.46(1)$, and $T_c = 5.32(1)$ K indicates that Ce$_2$Te$_5$ shows a three-dimensional magnetic critical behavior. Moreover, the Hall resistivity ρ_{xy} indicates that Ce$_2$Te$_5$ is a multiband system with a relatively high electron mobility ∼2900 cm^2 V^{-1} s^{-1} near T_c, providing further opportunities for future device applications.

DOI: 10.1103/PhysRevMaterials.6.094407

I. INTRODUCTION

Layered van der Waals (vdW) materials have attracted widespread attention due to the exotic quantum states they exhibit, such as correlated insulating, ferromagnetic, and superconducting states in "twisted" bilayer graphene [1–3], or quantum criticality in twisted transition metal dichalcogenides [4]. The discovery of intrinsic long-range magnetic order in monolayer CrI$_3$ and bilayer CrGeTe$_3$ has opened up new avenues of research into magnetism in the two-dimensional (2D) limit [5,6] as well as integration of 2D magnetic layers for control of magnetism by gating or other electrical means in devices [7–13]. Accordingly, several other 3d-electron vdW magnets, such as FePS$_3$, Fe$_3$GeTe$_2$, VSe$_2$, VI$_3$, CrTe$_2$, and MnSe$_2$, have been extensively investigated [14–20]. In contrast, very few f-electron vdW magnets have been studied (e.g., CeSiI [21], EuC$_6$ [22–24], and GdTe$_3$ [25]). Many f-electron materials exhibit significant hybridization between the f-electrons and conduction electrons, leading to highly correlated quantum states with narrow f-bands near the Fermi level; thus, 2D f-electron vdW materials may be highly tunable with modest amounts of pressure, uniaxial strain, or magnetic field, making them promising candidates for discovering and exploring unusual quantum states.

The family of rare-earth telluride RTe$_x$ (R = rare-earth element; x = 2, 2.5, and 3) adopts a layered crystal structure, consisting of square planar Te layers and corrugated RTe slabs. The RTe slabs are semiconducting and responsible for magnetism, while the Te layers form 2D conducting bands; thus RTe$_x$ exhibits highly anisotropic transport and magnetic properties [26–31]. Among this series, CeTe$_2$ and CeTe$_3$ crystallize in the layered Cu$_2$Sb-type tetragonal (space group: $P4/nmm$) structure and NdTe$_3$-type weakly orthorhombic (space group: $Cmcm$) structure, respectively, with localized Ce^{3+} magnetic moments. CeTe$_2$ contains a single layer of

Te and undergoes an antiferromagnetic (AFM) transition at $T_N = 4.3$ K [32–35]. At 2 K, a metamagnetic transition to a field-induced ferromagnetic (FM) state with an easy c axis occurs at a small magnetic field of 0.06 T. The resistivity shows a sharp peak at $T_\rho = 6$ K well above T_N with a large negative magnetoresistance (MR) [34–38] arising from magnetic-polaron and/or short-range FM ordering. Neutron diffraction measurements indicate a down-up-up-down AFM configuration along the c axis with FM Ce double layers above and below the Te layer in CeTe$_2$ [39–43]. CeTe$_3$ contains double layers of Te connected via weak vdW force; it exhibits two AFM transitions at $T_{N1} = 3.1$ K and $T_{N2} = 1.3$ K with nonparallel easy axes that are perpendicular to the layer stacking direction, i.e., strongly easy-plane character [44–47].

Layered Ce$_2$Te$_5$ can be considered as a combination of CeTe$_2$ and CeTe$_3$ (Fig. 1), consisting of alternating single and double Te layers stacked along the b axis of the orthorhombic unit cell and separated by CeTe slabs [48]. Ce$_2$Te$_5$ crystallizes in a weakly orthorhombic structure, similar to CeTe$_3$, with two Ce sites either adjacent to the double layers of Te (Ce1) or to the monolayer of Te (Ce2). Chen *et al.* reported three magnetic transitions at 5.1, 2.3, and 0.9 K in Ce$_2$Te$_5$ single crystals [48].

In this study, we report the physical properties of single crystals of Ce$_2$Te$_5$, including magnetic susceptibility, magnetization, specific heat, and longitudinal and Hall resistivity measurements. An additional magnetic transition at ∼0.4 K was observed, where the resistivity features a weak kink and the specific heat exhibits a peak. When magnetic field is applied along the b axis, the resistivity shows that the first transition $T_c \sim 5.2$ K broadens and shifts to higher temperatures, consistent with FM ordering; however, the second and third transitions at $T_2 = 2.1$ K and $T_3 = 0.9$ K move to lower temperatures. The critical exponents obtained around T_c indi-
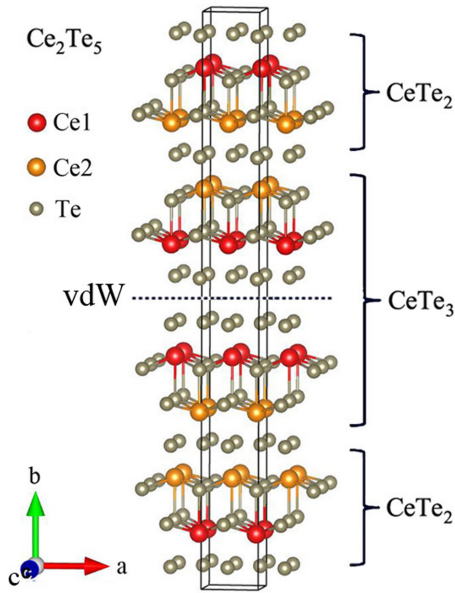
FIG. 1. Crystal structure of the van der Waals (vdW) magnet Ce_2Te_5 with alternating stacking of $CeTe_2$ and $CeTe_3$ along the b-axis.

cate that Ce_2Te_5 shows a three-dimensional magnetic critical behavior. Furthermore, the Hall effect suggests that Ce_2Te_5 is a multiband system with a relatively high electron mobility around T_c.

II. METHODS

A. Experimental details

Single crystals of Ce_2Te_5 with typical dimensions of $3 \times 3 \times 0.1$ mm^3 were grown by a RbCl/LiCl flux [48]. The crystallographic structure of Ce_2Te_5 was verified at room temperature by a Bruker D8 Venture single-crystal x-ray diffractometer equipped with Mo radiation. X-ray diffraction analysis shows that Ce_2Te_5 crystallizes in the orthorhombic space group $Cmcm$ (No. 63) with lattice parameters $a \sim c \approx 4.42$ Å and $b \approx 44.17$ Å, in agreement with a previous report [48].

The magnetization was measured in a Quantum Design Magnetic Property Measurement System (MPMS) from 2 to 350 K up to magnetic fields $\mu_0 H = 6$ T, and μ_0 is magnetic permeability in vacuum. For critical analysis, the reported internal magnetic field ($\mu_0 H_{int}$) has been corrected, $\mu_0 H_{int} = \mu_0 H - NM$, where $\mu_0 H$ is the applied magnetic field, M is the measured magnetization, and $N \sim 0.95$ is the demagnetization factor. The specific heat was measured using a Quantum Design Physical Property Measurement System (PPMS) from 0.35 to 20 K that utilizes a quasia-diabatic thermal relaxation technique. The longitudinal and Hall resistivity were measured in a PPMS using standard four-probe configurations with the current flowing in the ac-plane and the magnetic field applied along the b-axis. The Hall resistivity $\rho_{xy}(\mu_0 H)$ was calculated by the difference of transverse resistivity measured at positive and negative fields, i.e., $\rho_{xy}(\mu_0 H) = (\rho_{H+} - \rho_{H-})/2$, so as to effectively elimi-

nate the longitudinal resistivity contribution due to voltage probe misalignment.

B. Scaling analysis

A second-order phase transition around the Curie temperature T_c is characterized by a set of interrelated critical exponents β, γ, δ, and a magnetic equation of state [49]. The critical exponents β and γ are associated with the spontaneous magnetization M_s and the inverse initial susceptibility χ_{ini}^{-1}, below and above T_c, respectively, while δ is the critical isotherm exponent. The definitions of β, γ, and δ from magnetization measurement are given below:

$$M_s(T) = M_0(-\varepsilon)^\beta, \ \varepsilon < 0, \ T < T_c, \tag{1}$$

$$\chi_{ini}^{-1}(T) = (\mu_0 h_0/m_0)\varepsilon^\gamma, \ \varepsilon > 0, \ T > T_c, \tag{2}$$

$$M = D(\mu_0 H_{int})^{1/\delta}, \ T = T_c, \tag{3}$$

where $\varepsilon = (T - T_c)/T_c$ is the reduced temperature, and M_0, $\mu_0 h_0/m_0$, and D are critical amplitudes [50].

The magnetic equation of state in the critical region ($\varepsilon \leqslant 0.1$) can be expressed as

$$M(\mu_0 H_{int}, \varepsilon) = \varepsilon^\beta f_\pm(\mu_0 H_{int}/\varepsilon^{\beta+\gamma}), \tag{4}$$

where f_- for $T < T_c$ and f_+ for $T > T_c$, respectively, are regular functions. Equation (4) can be further written in terms of scaled magnetization $m \equiv \varepsilon^{-\beta} M(\mu_0 H_{int}, \varepsilon)$ and scaled field $\mu_0 h \equiv \varepsilon^{-(\beta+\gamma)} \mu_0 H_{int}$ as

$$m = f_\pm(\mu_0 h). \tag{5}$$

This suggests that for true scaling relations and the right choice of β, γ, and δ values, the scaled m and $\mu_0 h$ will fall on universal curves above T_c and below T_c, respectively.

III. RESULTS AND DISCUSSION

Figure 2(a) shows the temperature dependence of magnetic susceptibility $\chi(T)$ measured in $\mu_0 H = 0.1$ T applied parallel and perpendicular to the b-axis. A rapid upturn in $\chi(T)$ at low temperature is observed for both field directions, indicating a FM transition. In this field, the zero-field-cooled (ZFC) and field-cooled (FC) data overlap well for each orientation. The temperature dependence of inverse susceptibility $1/\chi(T)$ is plotted in Fig. 2(b). A linear fit from 200 to 300 K to a Curie-Weiss form, $\chi = C/(T - \theta)$, where C is the Curie constant and θ is the paramagnetic Curie-Weiss temperature, gives $\theta = 9.6$ K for $H \parallel b$ and -18.0 K for $H \perp b$, respectively. The positive value of θ for $H \parallel b$ is consistent with a dominant FM interaction, while the negative θ for $H \perp b$ suggests a dominant AFM interaction. The derived effective moment $\mu_{eff} = 2.56\mu_B$/Ce for $H \parallel b$ and $2.52\mu_B$/Ce for $H \perp b$, respectively, are very close to Hund's value for Ce^{3+} of $2.54\mu_B$. It should be noted that the high-temperature anisotropy and deviation from Curie-Weiss behavior with decreasing temperature may be attributed to a crystalline electric field (CEF) effect as explained below. Figure 2(c) shows the low temperature $\chi(T)$ measured in a small field of $\mu_0 H = 1$ mT. In the ordered state, $\chi(T)$ for $H \parallel b$ is 20 times larger than that of $H \perp b$, indicating a large magnetic anisotropy. The
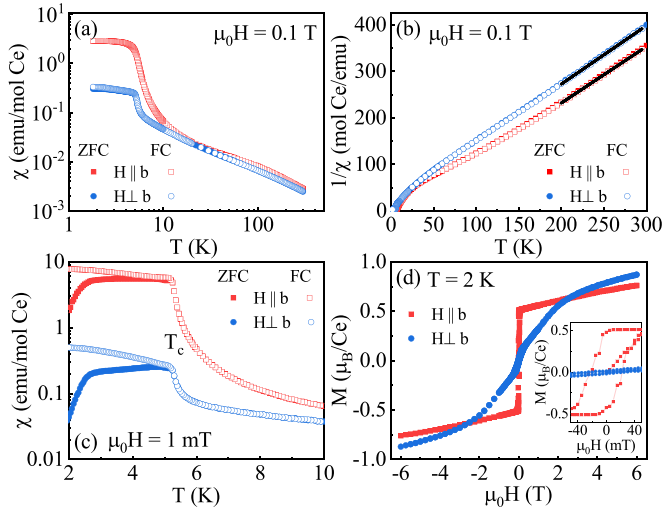
FIG. 2. Temperature dependence of (a) magnetic susceptibility $\chi(T)$, defined as $M/\mu_0 H$, and (b) inverse magnetic susceptibility $1/\chi(T)$ of Ce_2Te_5 measured in magnetic field of $\mu_0 H = 0.1$ T applied parallel and perpendicular to the b-axis in zero-field-cooled (ZFC) and field-cooled (FC) modes. The solid lines are linear fits to the data. (c) The low temperature $\chi(T)$ measured in a low magnetic field of $\mu_0 H = 1$ mT. (d) Field dependence of magnetization $M(\mu_0 H)$ of Ce_2Te_5 measured at $T = 2$ K.

bifurcation of ZFC and FC curves below $T_c \approx 5.2$ K is likely due to a FM domain effect. Figure 2(d) displays the isothermal magnetization measured at 2 K. The magnetization $M(H \parallel b)$ rapidly saturates to $\sim 0.5\mu_B$/Ce at 40 mT, whereas $M(H \perp b)$ gradually increases. It is interesting that $M(H \perp b)$ increases up to a higher value than $M(H \parallel b)$ above 2.5 T [Fig. 2(d)], in line with the previous results [48], indicating that the magnetic order is more complex than simple ferromagnetism in Ce_2Te_5. A similar feature was also observed in bulk CrI_3 [12]. As shown in the inset of Fig. 2(d), a clear hysteresis loop with coercive field $\mu_0 H_c \approx 20$ mT is observed for $H \parallel b$, indicating soft ferromagnetism with an easy b axis.

As shown in Fig. 3, the anisotropic magnetic susceptibilities can be modeled with a CEF Hamiltonian for Ce^{3+} of total angular momentum $J = 5/2$. In Ce_2Te_5, due to a and c being accidentally degenerate in the orthorhombic $Cmcm$ crystal structure, the local Ce point group has C_{4v} symmetry with the fourfold rotational axis along the crystallographic b-axis. The resultant CEF Hamiltonian contains three CEF parameters B_n^m with corresponding Steven's operators $\hat{O}_m^n$ [51] as

$$H_{CEF} = B_2^0 \hat{O}_2^0 + B_4^0 \hat{O}_4^0 + B_4^4 \hat{O}_4^4, \qquad (6)$$

which produces three Kramers doublets. In the C_{4v} point group and J, m_j basis, these doublets are labeled Γ_6 with $m_j = \pm 1/2$ components or Γ_7^1/Γ_7^2 with mixed $m_j = \pm 5/2$ and $\pm 3/2$ components. Magnetic susceptibility of the CEF Hamiltonian was calculated using Mantid Plot [52] with an additional temperature-independent χ_0 term and effective mean-field exchange interactions $\Theta_\perp$ and $\Theta_\parallel$. An effective susceptibility was calculated as $\chi_{eff} = \chi_{CEF}^{calc}/(1 - \Theta \chi_{CEF}^{calc})$ and compared to the observed $\chi_{obs} = \chi - \chi_0$, where χ_0 is a temperature-independent contribution. The overall fit was determined by minimizing $X^2 = (\chi_{calc} - \chi_{obs})^2/\chi_{calc}$
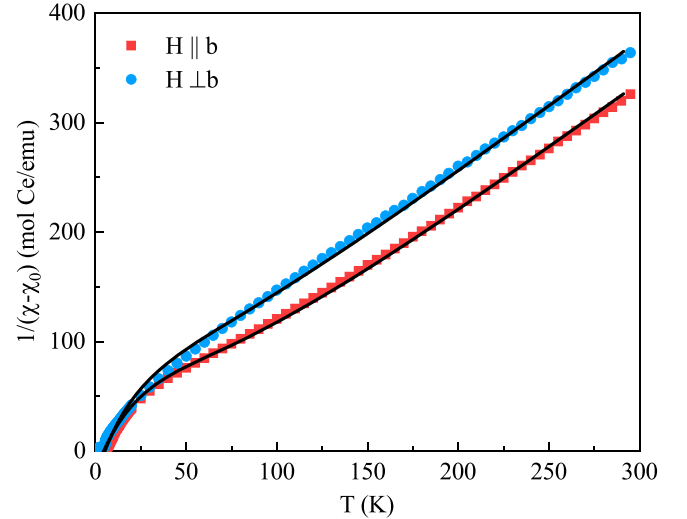

FIG. 3. Temperature dependence of $1/(\chi - \chi_0)(T)$ of Ce_2Te_5 with a crystalline electric field (CEF) model fit (solid lines) as explained in the main text.

with a final $X^2 = 15.8$ and extracted parameters $B_2^0 = -0.390\,03$ meV, $B_4^0 = 0.065\,95$ meV, $B_4^4 = -0.219\,87$ meV, $\chi_0 = -0.000\,195$ emu mol^{-1}, $\Theta_\perp = 24.74$ K, and $\Theta_\parallel = 18.81$ K. The ground-state doublet is $\Gamma_7^1 = 0.396| \pm 5/2\rangle + 0.918| \mp 3/2\rangle$, the first excited state doublet $\Gamma_7^2 = 0.918| \pm 5/2\rangle - 0.396| \mp 3/2\rangle$ is at 16.23 meV, and the second excited state doublet $\Gamma_6 = | \pm 1/2\rangle$ is at 24.67 meV. The ground-state doublet has projected g factors $g_\perp = 1.393$ and $g_\parallel = 1.497$, respectively. Taking $J_{eff} = 1/2$ for the ground-state doublet, the expected saturated moment $gJ\mu_B$ is 0.697 μ_B/Ce for $H \perp b$ and 0.749 μ_B/Ce for $H \parallel b$, in reasonable agreement with the magnetization at 2 K and 6 T, $M_{H \perp b} = 0.87\mu_B$/Ce and $M_{H \parallel b} = 0.76\mu_B$/Ce.

To understand the nature of the FM transition in Ce_2Te_5, one approach is to study in detail the critical exponents around T_c. Magnetization isotherms along the easy b-axis were measured from 4.6 to 6 K at intervals of 0.1 K. An Arrott plot of M^2 versus $\mu_0 H_{int}/M$ at various temperatures is displayed in Fig. 4(a). In the mean-field description of the magnetization near T_c, curves in the Arrott plot should be a series of parallel straight lines with the one passing through the origin indicating the T_c [53–55]. It is clear that mean-field critical exponents do not work for Ce_2Te_5, as illustrated by a set of curved lines shown in Fig. 4(a). According to the Arrott-Noakes equation of state $(\mu_0 H_{int}/M)^{1/\gamma} = a\varepsilon + bM^{1/\beta}$ [55], where a and b are constants, a modified Arrott plot should be used to obtain the critical exponents. β and γ can be obtained self-consistently. After selecting β and γ, the linear extrapolation from the high-field region to the intercepts with the axes $M^{1/\beta}$ and $(\mu_0 H_{int}/M)^{1/\gamma}$ yields the values of $M_s(T)$ and $\chi_{ini}^{-1}(T)$. A new set of β and γ can be obtained by fitting data following Eqs. (1) and (2), which can be used to reconstruct a new modified Arrott plot. This procedure is then repeated until the values of β and γ are stable [56].

Figure 4(b) presents the final $M_s(T)$ and $\chi_{ini}^{-1}(T)$ with the fitted curves. Critical exponents $\beta = 0.30(2)$, $\gamma = 0.99(5)$, and $T_c = 5.32(1)$ K are obtained. Figure 4(c) exhibits the
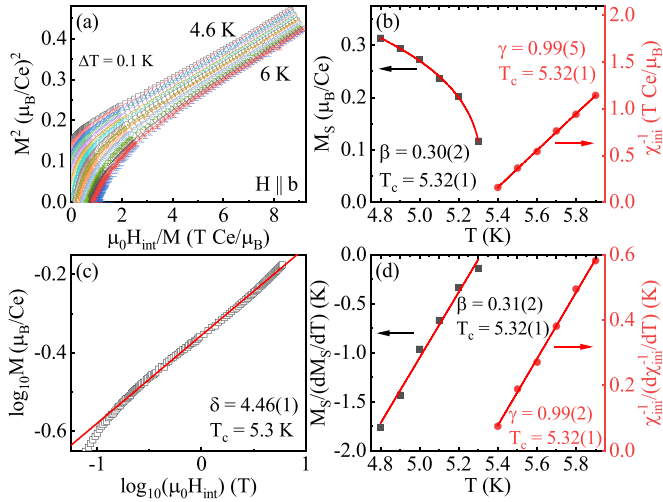
FIG. 4. (a) Arrott plots of M^2 vs $\mu_0 H_{int}/M$ around T_c for Ce_2Te_5 with $H \parallel b$. (b) Temperature dependence of the spontaneous magnetization M_s (left) and the inverse initial susceptibility χ_{ini}^{-1} (right) with fitted curves for Ce_2Te_5 explained in the main text. (c) Isotherm in $\log_{10}M$-$\log_{10}(\mu_0 H_{int})$ measured at $T_c = 5.3$ K, along with a linear fit to the data. (d) Kouvel-Fisher plots of $M_s(dM_s/dT)^{-1}$ (left) and $\chi_{ini}^{-1}(d\chi_{ini}^{-1}/dT)^{-1}$ (right), along with linear fits to the data.

field dependence of magnetization of Ce_2Te_5 at $T_c = 5.3$ K in a $\log_{10}M$-$\log_{10}(\mu_0 H_{int})$ plot, yielding $\delta = 4.46(1)$ from Eq. (3). In comparison to the theoretical prediction based on the Widom relation [57],

$$\delta = 1 + \frac{\gamma}{\beta}, \qquad (7)$$

the derived $\delta = 4.3(1)$ is close to that obtained in Fig. 4(c). In addition, critical exponents can also be determined according to the Kouvel-Fisher (KF) method [59]:

$$\frac{M_s(T)}{dM_s(T)/dT} = \frac{T - T_c}{\beta}, \qquad (8)$$

$$\frac{\chi_{ini}^{-1}(T)}{d\chi_{ini}^{-1}(T)/dT} = \frac{T - T_c}{\gamma}. \qquad (9)$$

$M_s(T)/[dM_s(T)/dT]$ and $\chi_{ini}^{-1}(T)/[d\chi_{ini}^{-1}(T)/dT]$ are linear functions of temperature with slopes of $1/\beta$ and $1/\gamma$, respectively. As shown in Fig. 4(d), the linear fits give $\beta = 0.31(2)$, $\gamma = 0.99(2)$, and $T_c = 5.32(1)$ K, which are consistent with those generated by the modified Arrott plot.

Following Eq. (5), the scaled $m = M|\varepsilon|^{-\beta}$ versus scaled $\mu_0 h = \mu_0 H_{int}|\varepsilon|^{-(\gamma+\beta)}$ is plotted in Fig. 5(a). All the data collapse reasonably well into two separate branches, one below T_c and another above T_c. The scaling equation of state also takes another form:

$$\frac{\mu_0 H_{int}}{M^\delta} = k\left[\frac{\varepsilon}{(\mu_0 H_{int})^{1/\beta}}\right], \qquad (10)$$

where $k(x)$ is the scaling function. Figure 5(b) shows $M(\mu_0 H_{int})^{-1/\delta}$ versus $\varepsilon(\mu_0 H_{int})^{-1/(\beta\delta)}$ for Ce_2Te_5, where the experimental data collapse reasonably onto a single curve, and T_c locates at the zero point of the horizontal axis. The well-scaled curves confirm reliability of the obtained critical exponents. Figure 5(c) presents the derived magnetic en-
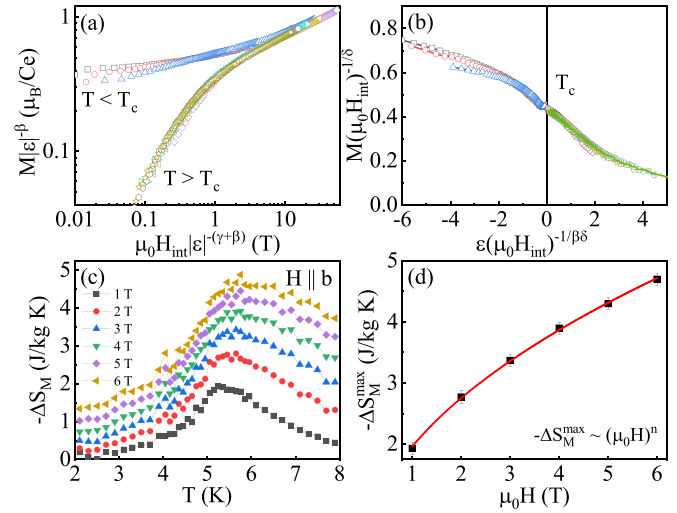

FIG. 5. (a) The scaling plots of normalized magnetization m as a function of normalized field $\mu_0 h$ below and above T_c for Ce_2Te_5. (b) Scaled magnetization $M(\mu_0 H_{int})^{-1/\delta}$ vs scaled field $\varepsilon(\mu_0 H_{int})^{-1/\beta\delta}$. (c) The magnetic entropy change $-\Delta S_M$ obtained from magnetization at various magnetic fields along the b-axis. (d) Field dependence of the maximum magnetic entropy change $-\Delta S_M^{max}$ with a power-law fit.

tropy change $-\Delta S_M = \int_0^{\mu_0 H}[\partial M(T, \mu_0 H)/\partial T]_{\mu_0 H}d(\mu_0 H)$ [60], which shows a broad peak centered near T_c. The peak value monotonically increases with increasing field, reaching 4.7(1) J kg^{-1} K^{-1} in 6 T. The field dependence of $-\Delta S_M^{max}$ follows a power law $-\Delta S_M^{max} \propto (\mu_0 H)^n$ with $n = 1 + (\beta - 1)/(\beta + \gamma)$ [61–65]. Fitting of $-\Delta S_M^{max}$ gives $n = 0.49(1)$, which is close to the calculated value of 0.46(1), further verifying the reliability of the obtained critical exponents.

Taroni *et al.* pointed out that the value of β for a 2D magnet should be within a window $0.1 \leqslant \beta \leqslant 0.25$ [66]. The value of ~ 0.31 obtained here indicates a clear 3D behavior in Ce_2Te_5. As we can see, the critical exponent β of Ce_2Te_5 is close to the theoretical value ($\beta = 0.325$) of the 3D Ising model (Table I), consistent with the large anisotropy in magnetization below T_c [Fig. 2(d)]. However, the value of $\gamma \sim 1.0$ of Ce_2Te_5 deviates from $\gamma = 1.24$ of the 3D Ising model, which might be arising from the long-range Ruderman-Kittel-Kasuya-Yosida (RKKY) interactions.

Having delineated salient features of the FM state around T_c, we now turn to an investigation of electrical transport properties. Figure 6(a) shows the temperature dependence of ac-plane resistivity $\rho(T)$ of Ce_2Te_5, a typical metallic behavior with a slope change around 100 K. This might be related to the hybridization between local moments and conduction electrons, and the presence of a CEF doublet near 190 K. The low-temperature $\rho(T)$ of Ce_2Te_5 displays four consecutive transitions at 5.2, 2.1, 0.9, and 0.4 K [inset in Fig. 6(a)]. The first transition temperature corresponds well to the FM transition (T_c) in $\chi(T)$ [Fig. 2(a)]. Below T_c and T_2, $\rho(T)$ decreases more rapidly due to a decrease of spin disorder scattering; however, $\rho(T)$ shows a rapid upturn below T_3 and a weak kink at T_4 that suggest the opening of a small gap possibly due to a spin-density wave. The specific heat divided by temperature, C_p/T [Fig. 6(b)], shows peaks at 5.2, 2.1, and 0.9 K and an

TABLE I. Comparison of critical exponents of Ce_2Te_5 with different theoretical models. MAP, KFP, and CI represent the modified Arrott plot, the Kouvel-Fisher plot, and the critical isotherm, respectively.

	Reference	Technique	T_c	β	γ	δ
Ce_2Te_5	This work	MAP	5.32(1)	0.30(2)	0.99(5)	4.30(5)
		KFP	5.32(1)	0.31(2)	0.99(2)	4.2(1)
		CI	5.3			4.46(1)
2D Ising	[58]	Theory		0.125	1.75	15.0
Mean field	[59]	Theory		0.5	1.0	3.0
3D Heisenberg	[59]	Theory		0.365	1.386	4.8
3D Ising	[67]	Theory		0.325	1.24	4.82
3D XY	[68]	Theory		0.345	1.316	4.81
Tricritical mean field	[69]	Theory		0.25	1.0	5.0

upturn toward 0.4 K that are consistent with the four transitions observed in $\rho(T)$. The electronic entropy S_{4f} [inset in Fig. 6(b)] is determined by subtracting a βT^3 phonon contribution from C_p/T (obtained from a linear fit to $C_p/T = \gamma + \beta T^2$ from 9 to 10 K), and integration of the resulting $4f$ contribution to the specific heat $S_{4f} = \int (C_{4f}/T) dT$. The value of S_{4f} approaches $R\ln 2$ at 10 K, indicating a crystal-field doublet ground state in Ce_2Te_5. About 75% of $R\ln 2$ of entropy is released below T_c and about 30% of $R\ln 2$ is released below

T_2. One plausible scenario is that one Ce sublattice orders ferromagnetically below T_c, while the other Ce sublattice orders antiferromagnetically below T_2. This scenario is consistent with the roughly equal amount of entropy released below T_c and T_2 [Fig. 6(b), inset], the soft ferromagnetic response of $M(H)$ at $T = 2$ K below T_2, the field dependence of the ordering temperatures discussed below, and the competition of magnetic interactions in Ce_2Te_5. Alternatively, magnetic coupling between the two magnetic Ce sublattices may give rise to interesting magnetically ordered states, such as ferrimagnetism below T_c, coexistent FM and AFM states at 2 K [see Fig. 2(d)], or incommensurate ordered states. Further neutron scattering and/or μSR measurements will be useful to determine the nature of the magnetically ordered states and their underlying magnetic interactions in Ce_2Te_5.

With increasing magnetic fields applied along the b axis, as shown in Fig. 7(a), the first transition T_c broadens and
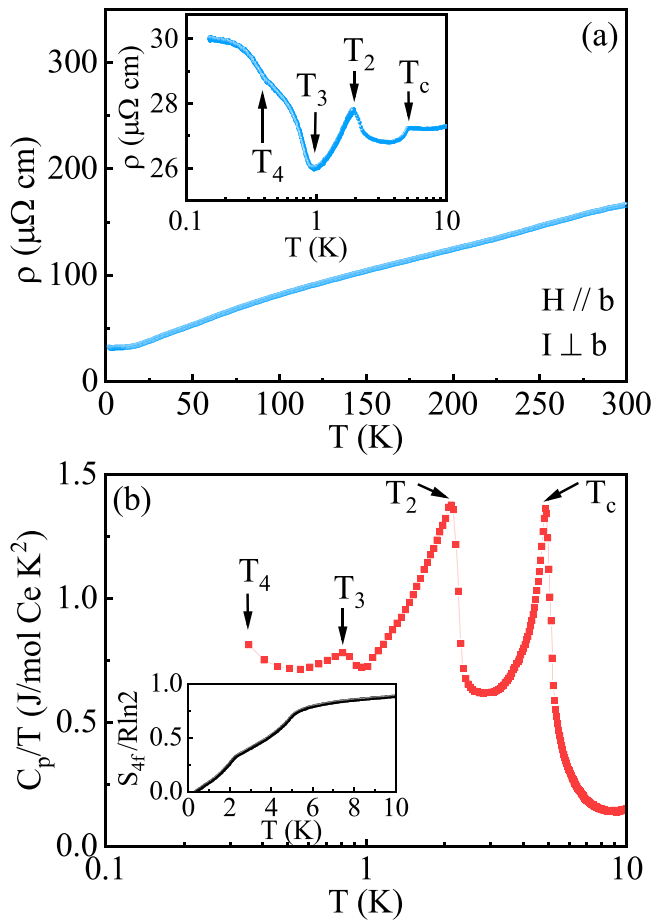

FIG. 6. Temperature dependence of (a) in-plane electrical resistivity $\rho(T)$ and (b) specific heat C_p/T of Ce_2Te_5 in zero field. The inset in (b) shows the electronic entropy $S_{4f}(T)/R\ln 2$ of Ce_2Te_5.
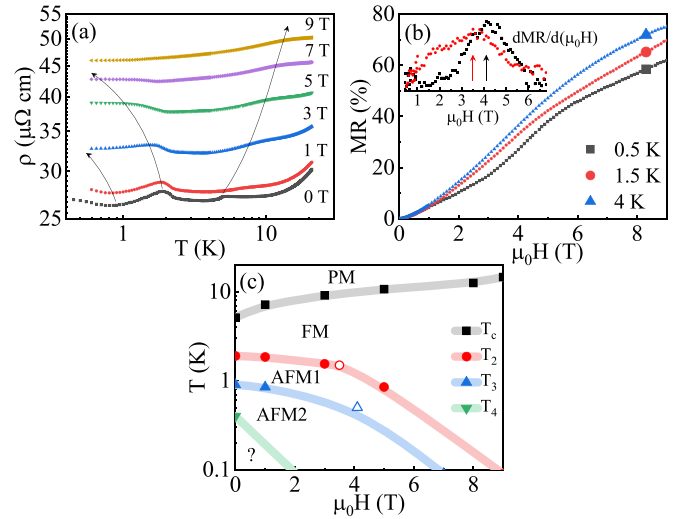
FIG. 7. (a) Magnetic-field variations of in-plane electrical resistivity $\rho(T)$ for $I \perp b$ and $H \parallel b$ for a single crystal of Ce_2Te_5. The lines are guides to the eye. (b) The longitudinal magnetoresistance (MR) of Ce_2Te_5 at indicated temperatures. The inset shows $dMR/d(\mu_0 H)$ curves at 0.5 and 1.5 K. (c) The magnetic phase diagram constructed from transport measurements (solid symbols from ρ; open symbols from MR). PM, FM, and AFM represent paramagnetic, ferromagnetic, and antiferromagnetic phases, respectively. The lines are guides to the eye.

FIG. 8. The field dependence of Hall resistivity $\rho_{xy}(\mu_0 H)$ at various (a) high and (b) low temperatures with $I \perp b$ and $H \parallel 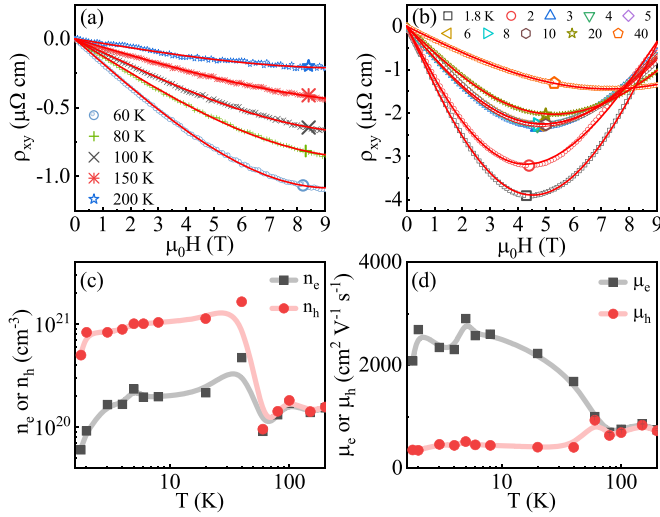b$ for a single crystal of Ce$_2$Te$_5$. The lines in (a) and (b) are fits of the two-band model to the data as explained in the main text. Part (c) shows the derived electron concentration n_e and hole concentration n_h, and (d) shows electron mobility μ_e and hole mobility μ_h.

shifts to higher temperature, confirming it is a FM transition. T_2 and T_3, however, move to lower temperature and are finally suppressed in high fields, indicating an AFM character. Figure 7(b) shows the field dependence of longitudinal magnetoresistance (MR) measured at 0.5, 1.5, and 4 K. The MR at 4 K shows a relatively large positive value of 75% in $\mu_0 H = 9$ T. In addition, an inflection was observed at low temperatures. As depicted in the inset of Fig. 7(b), a peak in $d\mathrm{MR}/d(\mu_0 H)$ indicates a critical field of $\sim$4.1 T at 0.5 K and 3.5 T at 1.5 K, respectively, which are associated with the T_2 and T_3 transitions. Based on these transport measurements, the magnetic phase $(T - \mu_0 H)$ diagram of Ce$_2$Te$_5$ is summarized in Fig. 7(c). The contribution of the interlayer magnetic interactions between CeTe$_2$ and CeTe$_3$ likely generates complex magnetic interactions in Ce$_2$Te$_5$. The nature of T_4 at the lowest temperature needs further investigation, and neutron scattering measurements are required to determine the CEF levels and the magnetic structure of Ce$_2$Te$_5$.

To shed light on the transport carriers in Ce$_2$Te$_5$, we further measured the field dependence of Hall resistivity $\rho_{xy}(\mu_0 H)$ of Ce$_2$Te$_5$ with current flowing in the ac-plane and the field applied along the b-axis at various temperatures, as shown in Figs. 8(a) and 8(b). The Hall coefficient $\rho_{xy}/(\mu_0 H)$ is negative at high temperatures, indicating dominant electron-like carriers. With decreasing temperature, ρ_{xy} exhibits nonlinear behavior below 60 K, and the shape of ρ_{xy} changes significantly below 40 K, becoming parabolic at low temperatures. These observations suggest that Ce$_2$Te$_5$ is a multiband system, as has been observed in a related compound GdTe$_3$ [25].

Assuming a two-band model, the Hall resistivity is expressed as

$$\rho_{xy} = \frac{\mu_0 H}{e} \frac{(n_h \mu_h^2 - n_e \mu_e^2) + (n_h - n_e)(\mu_e \mu_h \mu_0 H)^2}{(n_h \mu_h + n_e \mu_e)^2 + (n_h - n_e)^2 (\mu_e \mu_h \mu_0 H)^2}, \tag{11}$$

where e is the elementary charge; n_e and n_h are the electron and hole carrier concentrations, respectively; and μ_e and μ_h are the electron and hole carrier mobilities, respectively. The derived fitting parameters n_e, n_h, μ_e, and μ_h are plotted in Figs. 8(c) and 8(d), respectively, where the electron and hole carriers are almost compensated at high temperatures and become uncompensated below 60 K. The carrier concentration is of the order of 10^{20}–10^{21} cm^{-3} [Fig. 7(c)]. The hole mobility μ_h is $\sim$350–930 cm^2/V s and is weakly temperature-dependent; however, μ_e increases abruptly below 60 K and features a relatively large value of $\sim$2900 cm^2/V s near T_c. This high electron mobility in Ce$_2$Te$_5$, a vdW layered and magnetically ordered material, is larger than that of some other rare-earth materials such as YbMn(Bi, Sb)$_2$ and EuMnBi$_2$ [70–72], and it provides further opportunities for future device applications.

IV. CONCLUSIONS

In summary, we studied the magnetic, transport, and thermodynamic properties of the f-electron vdW magnet Ce$_2$Te$_5$, and we summarized its magnetic phase diagram. Four magnetic transitions were observed at $T_c = 5.2$, $T_2 = 2.1$, $T_3 = 0.9$, and $T_4 = 0.4$ K. Critical exponents in the vicinity of the FM transition are determined to be $\beta = 0.31(2)$, $\gamma = 0.99(2)$, $\delta = 4.46(1)$, and $T_c = 5.32(1)$ K, indicating that Ce$_2$Te$_5$ shows a three-dimensional magnetic critical behavior. A crystal electric field model of the magnetic susceptibility suggests that the ground state Γ_7^1 doublet has a dominant $|3/2\rangle$ character with excited Γ_7^2 and Γ_6 states at $\sim$16 and 25 meV, respectively. Further neutron scattering or x-ray absorption spectroscopy measurements will be needed to confirm this CEF scheme. The Hall resistivity analysis indicates that Ce$_2$Te$_5$ is a multiband system with a relatively high electron mobility around T_c. Furthermore, with rapid developments in the field of 2D materials, we expect our experimental work to stimulate broad interest for exploring its magnetic and transport properties in the 2D limit.

ACKNOWLEDGMENTS

[1] Y. Cao, V. Fatemi, A. Demir, S. Fang, S. L. Tomarken, J. Y. Luo, J. D. Sanchez-Yamagishi, K. Watanabe, T. Taniguchi, E. Kaxiras, R. C. Ashoori, and P. Jarillo-Herrero, Correlated insulator behaviour at half-filling in magic-angle graphene superlattices, Nature (London) **556**, 80 (2018).

[2] Y. Cao, V. Fatemi, S. Fang, K. Watanabe, T. Taniguchi, E. Kaxiras, and P. Jarillo-Herrero, Unconventional superconductivity in

magic-angle graphene superlattices, Nature (London) **556**, 43 (2018).

[3] M. Yankowitz, S. Chen, H. Polshyn, Y. Zhang, K. Watanabe, T. Taniguchi, D. Graf, A. F. Young, and C. R. Dean, Tuning superconductivity in twisted bilayer graphene, Science **363**, 1059 (2019).

[4] A. Ghiotto, E.-M. Shih, G. S. S. G. Pereira, D. A. Rhodes, B. Kim, J. Zang, A. J. Millis, K. Watanabe, T. Taniguchi, J. C. Hone, L. Wang, C. R. Dean, and A. N. Pasupathy, Quantum criticality in twisted transition metal dichalcogenides, Nature (London) **597**, 345 (2021).

[5] B. Huang, G. Clark, E. Navarro-Moratalla, D. R. Klein, R. Cheng, K. L. Seyler, D. Zhong, E. Schmidgall, M. A. McGuire, D. H. Cobden, W. Yao, D. Xiao, P. Jarillo-Herrero, and X. D. Xu, Layer-dependent ferromagnetism in a van der Waals crystal down to the monolayer limit, Nature (London) **546**, 270 (2017).

[6] C. Gong, L. Li, Z. L. Li, H. W. Ji, A. Stern, Y. Xia, T. Cao, W. Bao, C. Z. Wang, Y. Wang, Z. Q. Qiu, R. J. Cava, S. G. Louie, J. Xia, and X. Zhang, Discovery of intrinsic ferromagnetism in two-dimensional van der Waals crystals, Nature (London) **546**, 265 (2017).

[7] K. F. Mak, J. Shan, and D. C. Ralph, Probing and controlling magnetic states in 2D layered magnetic materials, Nat. Rev. Phys. **1**, 646 (2019).

[8] K. S. Burch, D. Mandrus, and J.-G. Park, Magnetism in two-dimensional van der Waals materials, Nature (London) **563**, 47 (2018).

[9] T. Song, X. Cai, M. W.-Y. Tu, X. Zhang, B. Huang, N. P. Wilson, K. L. Seyler, L. Zhu, T. Taniguchi, K. Watanabe, M. A. McGuire, D. H. Cobden, D. Xiao, W. Yao, and X. Xu, Giant tunneling magnetoresistance in spin-filter van der Waals heterostructures, Science **360**, 1214 (2018).

[10] Q. H. Wang, A. B.-Pinto, M. Blei, A. H. Dismukes, A. Hamo, S. Jenkins, M. Koperski, Y. Liu, Q.-C. Sun, E. J. Telford *et al.*, The magnetic genome of two-dimensional van der Waals materials, ACS Nano **16**, 6960 (2022).

[11] Y. Liu, L. Wu, X. Tong, J. Li, Y. Zhu, and C. Petrovic, Thickness-dependent magnetic order in CrI$_3$ single crystals, Sci. Rep. **9**, 13599 (2019).

[12] Y. Liu and C. Petrovic, Three-dimensional magnetic critical behavior in CrI$_3$, Phys. Rev. B **97**, 014420 (2018).

[13] Y. Liu and C. Petrovic, Critical behavior of quasi-two-dimensional semiconducting ferromagnet Cr$_2$Ge$_2$Te$_6$, Phys. Rev. B **96**, 054406 (2017).

[14] J. Lee, S. Lee, J. H. Ryoo, S. Kang, T. Y. Kim, P. Kim, C. Park, J. Park, and H. Cheong, Ising-type magnetic ordering in atomically thin FePS$_3$, Nano Lett. **16**, 7433 (2016).

[15] Y. J. Deng, Y. J. Yu, Y. C. Song, J. Z. Zhang, N. Z. Wang, Z. Y. Sun, Y. F. Yi, Y. Z. Wu, S. W. Wu, J. Y. Zhu, J. Wang, X. H. Chen, and Y. B. Zhang, Gate-tunable room-temperature ferromagnetism in two-dimensional Fe$_3$GeTe$_2$, Nature (London) **563**, 94 (2018).

[16] M. Bonilla, S. Kolekar, Y. Ma, H. C. Diaz, V. Kalappattil, R. Das, T. Eggers, H. R. Gutierrez, M. Phan, and M. Batzill, Strong room-temperature ferromagnetism in VSe$_2$ monolayers on van der Waals substrates, Nat. Nanotechnol. **13**, 289 (2018).

[17] X. Zhang, Q. Lu, W. Liu, W. Niu, J. Sun, J. Cook, M. Vaninger, P. F. Miceli, D. J. Singh, S. Lian, T. Chang, X. He, J. Du, L. He, R. Zhang, G. Bin, and Y. Xu, Room-temperature intrinsic ferromagnetism in epitaxial CrTe$_2$ ultrathin film, Nat. Commun. **12**, 2492 (2021).

[18] D. J. O'Hara, T. Zhu, A. H. Trout, A. S. Ahmed, Y. K. Luo, C. H. Lee, M. R. Brenner, S. Rajan, J. A. Gupta, D. W. McComb, and R. K. Kawakami, Room temperature intrinsic ferromagnetism in epitaxial manganese selenide films in the monolayer limit, Nano Lett. **18**, 3125 (2018).

[19] Y. Liu, M. Abeykoon, and C. Petrovic, Critical behavior and magnetocaloric effect in VI$_3$, Phys. Rev. Res. **2**, 013013 (2020).

[20] Y. Liu, V. N. Ivanovski, and C. Petrovic, Critical behavior of the van der Waals bonded ferromagnet Fe$_{3-x}$GeTe$_2$, Phys. Rev. B **96**, 144429 (2017).

[21] R. Okuma, C. Ritter, G. J. Nilsen, and Y. Okada, Magnetic frustration in a van der Waals metal CeSiI, Phys. Rev. Mater. **5**, L121401 (2021).

[22] I. S. Sokolov, D. V. Averyanov, O. E. Parfenov, I. A. Karateev, A. N. Taldnkov, A. M. Tokmachev, and V. G. Storchak, 2D ferromagnetism in europium/graphene bilayers, Mater. Horiz. **7**, 1372 (2020).

[23] I. S. Sokolov, D. V. Averyanov, O. E. Parfenov, A. N. Taldnkov, I. A. Karateev, A. M. Tokmachev, and V. G. Storchak, Two-dimensional ferromagnetism in Eu-intercalated few-layer graphene, J. Alloys Compd. **884**, 161078 (2021).

[24] I. S. Sokolov, D. V. Averyanov, F. Wilhelm, A. Rogalev, O. E. Parfenov, A. N. Taldnkov, I. A. Karateev, A. M. Tokmachev, and V. G. Storchak, Emerging 2D magnetic states in a graphene-based monolayer of EuC$_6$, Nano Res. **15**, 408 (2022).

[25] S. Lei, J. Lin, Y. Jia, M. Gray, A. Topp, G. Farahi, S. Klemenz, T. Gao, F. Rodolakis, J. L. McChesney, C. R. Ast, A. Yazdani, K. S. Burth, S. Wu, N. P. Ong, and L. M. Schoop, High mobility in a van der Waals layered antiferromagnetic metal, Sci. Adv. **6**, eaay6407 (2020).

[26] B. H. Min, J. H. Cho, H. J. Lee, C. W. Han, D. L. Kim, and Y. S. Kwon, Specific heat study in RTe$_2$ (R: La, Ce, Pr, Sm and Gd), Physica B: Condensed Matter **281&282**, 118 (2000).

[27] Y. S. Kwon and B. H. Min, Anisotropic transport properties in RTe$_2$ (R: La, Ce, Pr, Sm and Gd), Physica B: Condensed Matter **281&282**, 120 (2000).

[28] Y. S. Shin, C. W. Han, B. H. Min, H. J. Lee, C. H. Choi, Y. S. Kim, D. L. Kim, and Y. S. Kwon, Anisotropic magnetization in RTe$_2$ (R: Ce, Pr, Gd and Sm), Physica B **291**, 225 (2000).

[29] Y. Iyeiri, T. Okumura, C. Michioka, and K. Suzuki, Magnetic properties of rare-earth metal tritellurides RTe$_3$ (R = Ce, Pr, Nd, Gd, Dy), Phys. Rev. B **67**, 144417 (2003).

[30] N. Ru and I. R. Fisher, Thermodynamic and transport properties of YTe$_3$, LaTe$_3$, and CeTe$_3$, Phys. Rev. B **73**, 033101 (2006).

[31] N. Ru, J. H. Chu, and I. R. Fisher, Magnetic properties of the charge density wave compounds RTe$_3$ (R = Y, La, Ce, Pr, Nd, Sm, Gd, Tb, Dy, Ho, Er, and Tm), Phys. Rev. B **78**, 012410 (2008).

[32] Y. S. Kwon, T. S. Park, K. R. Lee, J. M. Kim, Y. Haga, and T. Suzuki, Transport and optical properties of CeTe$_2$, J. Magn. Magn. Mater. **140-144**, 1173 (1995).

[33] B. H. Min, H. Y. Choi, and Y. S. Kwon, Phys. B **312-313**, 203 (2002).

[34] M. Jung, B. Min, Y. Kwon, I. Oguro, F. Iga, T. Fujita, T. Ekino, T. Kasuya, and T. Takabatake, Anisotropic transport and magnetic properties and magnetic-polaron-like behavior in CeTe$_{2-x}$, J. Phys. Soc. Jpn. **69**, 937 (2000).

[35] M. H. Jung, K. Umeo, T. Fujita, and T. Takabatake, Competing interactions and anisotropic magnetoresistance in layered CeTe$_2$, Phys. Rev. B **62**, 11609 (2000).

[36] M. H. Jung, Y. S. Kwon, and T. Suzuki, Physica B **240**, 83 (1997).

[37] T. Kasuya, M. H. Jung, and T. Takabatake, J. Magn. Magn. Mater. **220**, 235 (2000).

[38] B. H. Min, E. D. Moon, H. J. Im, S. O. Hong, Y. S. Kwon, D. L. Kim, and H. C. Ri, Transport properties in low carrier system CeTe$_2$, Physica B **312-313**, 205 (2002).

[39] J. G. Park, I. P. Swainson, W. J. L. Buyers, M. H. Jung, and Y. S. Kwon, Physica B **241-243**, 684 (1997).

[40] J. G. Park, Y. S. Kwon, W. Kockelmann, M. J. Bull, I. P. Swainson, K. A. McEwen, and W. J. L. Buyers, Neutron scattering study of CeTe$_2$, Physica B: Condensed Matter **281&282**, 451 (2000).

[41] K. Stöwe, Crystal structure and magnetic properties of CeTe$_2$, J. Alloys Compd. **307**, 101 (2000)

[42] Z. S. Liu, J. G. Park, Y. S. Kwon, K. A. McEwen, and M. J. Bull, Crystal-field excitations and model calculations of CeTe$_2$, J. Magn. Magn. Mater. **256**, 151 (2003).

[43] J. H. Shim, S. J. Youn, M. S. Park, and B. I. Min, Electronic and magnetic structures of CeTe$_2$, J. Appl. Phys. **97**, 10A918 (2005).

[44] K. Deguchi, T. Okada, G. F. Chen, S. Ban, N. Aso, and N. K. Sato, Magnetic order of rare-earth tritelluride CeTe$_3$ at low temperature, J. Phys.: Conf. Ser. **150**, 042023 (2009).

[45] D. A. Zocco, J. J. Hamlin, T. A. Sayles, M. B. Maple, J. H. Chu, and I. R. Fisher, High-pressure, transport, and thermodynamic properties of CeTe$_3$, Phys. Rev. B **79**, 134428 (2009).

[46] R. Okuma, D. Ueta, S. Kuniyoshi, Y. Fujisawa, B. Smith, C. H. Hsu, Y. Inagaki, W. Si, T. Kawae, H. Lin, F. C. Chuang, T. Masuda, T. Kobayashi, and Y. Okada, Fermionic order by disorder in a van der Waals antiferromagnet, Sci. Rep. **10**, 15311 (2020).

[47] M. Watanabe, S. Lee, T. Asano, T. Ibe, M. Tokuda, H. Taniguchi, D. Ueta, Y. Okada, K. Kobayashi, and Y. Niimi, Quantum oscillations with magnetic hysteresis observed in CeTe$_3$ thin films, Appl. Phys. Lett. **117**, 072403 (2020).

[48] D. Chen, S. Zhang, H. X. Yang, J. Q. Li, and G. F. Chen, Magnetic and transport properties of a layered compound Ce$_2$Te$_5$, J. Phys.: Condens. Matter **29**, 265803 (2017).

[49] H. E. Stanley, *Introduction to Phase Transitions and Critical Phenomena* (Oxford University Press, London, 1971).

[50] M. E. Fisher, The theory of equilibrium critical phenomena, Rep. Prog. Phys. **30**, 615 (1967).

[51] K. Stevens, Matrix elements and operator equivalents connected with the magnetic properties of rare earth ions, Proc. Phys. Soc. A **65**, 209 (1952).

[52] O. Arnold, J.-C. Bilheux, J. M. Borreguero, A. Buts, S. I. Campbell, L. Chapon, M. Doucet, N. Draper, R. F. Leal, M. A. Gigg, V. E. Lynch, A. Markvardsen, D. J. Mikkelson, R. l. Mikkelson, R. Miller, K. Palmen, P. Parker, G. Passos, T. G. Perring, P. F.

[53] Peterson, S. Ren *et al.*, Mantid-data analysis and visualization package for neutron scattering and μSR experiments, Nucl. Instrum. Methods Phys. Res., Sect. A **764**, 156 (2014).

[53] A. Arrott, Criterion for ferromagnetism from observations of magnetic isotherms, Phys. Rev. **108**, 1394 (1957).

[54] S. K. Banerjee, On a generalised approach to first and second order magnetic transitions, Phys. Lett. **12**, 16 (1964).

[55] A. Arrott and J. Noakes, Approximate Equation of State For Nickel Near its Critical Temperature, Phys. Rev. Lett. **19**, 786 (1967).

[56] A. K. Pramanik and A. Banerjee, Critical behavior at paramagnetic to ferromagnetic phase transition in Pr$_{0.5}$Sr$_{0.5}$MnO$_3$: A bulk magnetization study, Phys. Rev. B **79**, 214426 (2009).

[57] L. Kadanoff, Scaling laws for Ising models near T_c, Phys. Phys. Fiz. **2**, 263 (1966).

[58] B. Widom, Degree of the critical isotherm, J. Chem. Phys. **41**, 1633 (1964).

[59] J. S. Kouvel and M. E. Fisher, Detailed magnetic behavior of nickel near its Curie point, Phys. Rev. **136**, A1626 (1964).

[60] J. Amaral, M. Reis, V. Amaral, T. Mendonc, J. Araujo, M. Sa, P. Tavares, and J. Vieira, Magnetocaloric effect in Er- and Eu-substituted ferromagnetic La-Sr manganites, J. Magn. Magn. Mater. **290-291**, 686 (2005).

[61] V. Franco, J. S. Blázquez, and A. Conde, Field dependence of the magnetocaloric effect in materials with a second order phase transition: A master curve for the magnetic entropy change, Appl. Phys. Lett. **89**, 222512 (2006).

[62] Y. Liu and C. Petrovic, Anisotropic magnetocaloric effect in single crystals of CrI$_3$, Phys. Rev. B **97**, 174418 (2018).

[63] Y. Liu and C. Petrovic, Critical behavior and magnetocaloric effect in Mn$_3$Si$_2$Te$_6$, Phys. Rev. B **98**, 064423 (2018).

[64] Y. Liu and C. Petrovic, Anisotropic magnetic entropy change in Cr$_2$X$_2$Te$_6$ (X = Si and Ge), Phys. Rev. Mater. **3**, 014001 (2019).

[65] Y. Liu, J. Li, J. Tao, Y. Zhu, and C. Petrovic, Anisotropic magnetocaloric effect in Fe$_{3-x}$GeTe$_2$, Sci. Rep. **9**, 13233 (2019).

[66] A. Taroni, S. T. Bramwell, and P. C. W. Holdsworth, Universal window for two-dimensional critical exponents, J. Phys.: Condens. Matter **20**, 275233 (2008).

[67] K. Huang, *Statistical Mechanics*, 2nd ed. (Wiley, New York, 1987).

[68] M. Phan, V. Franco, N. Bingham, H. Srikanth, N. Hur, and S. Yu, Tricritical point and critical exponents of La$_{0.7}$Ca$_{0.3-x}$Sr$_x$MnO$_3$ ($x = 0$, 0.05, 0.1, 0.2, 0.25) single crystals, J. Alloys Compd. **508**, 238 (2010).

[69] M. E. Fisher, S. K. Ma, and B. G. Nickel, Critical Exponents for Long-Range Interactions, Phys. Rev. Lett. **29**, 917 (1972).

[70] A. Wang, I. Zaliznyak, W. Ren, L. Wu, D. Graf, V. O. Garlea, J. B. Warren, E. Bozin, Y. Zhu, and C. Petrovic, Magnetotransport study of Dirac fermions in YbMnBi$_2$ antiferromagnet, Phys. Rev. B **94**, 165161 (2016).

[71] Y. Wang, S. Xu, L. Sun, and T. Xia, Quantum oscillations and coherent interlayer transport in a new topological Dirac semimetal candidate YbMnSb$_2$, Phys. Rev. Mater. **2**, 021201(R) (2018).

[72] A. F. May, M. A. McGuire, and B. C. Sales, Effect of Eu magnetism on the electronic properties of the candidate Dirac material EuMnBi$_2$, Phys. Rev. B **90**, 075109 (2014).